Isogeometric Modeling and Experimental Investigation of Moving-Domain Bridge Aerodynamics

Tore A. Helgedagsrud[1], Ido Akkerman[2], Yuri Bazilevs[3], Kjell M. Mathisen[4], and Ole A. Øiseth[5]

[1]Department of Structural Engineering, Norwegian University of Science and Technology
(NTNU), Richard Birkelands v 1a, NO-7491 Trondheim, Norway. Email:
tore.a.helgedagsrud@ntnu.no
[2]Department of Mechanical, Maritime and Materials Engineering, Delft University of
Technology, Mekelweg 2, 2628 CD Delft, Netherlands
[3]School of Engineering, Brown University, 184 Hope Street, Providence, RI 02912, USA
[4]Department of Structural Engineering, Norwegian University of Science and Technology
(NTNU), Richard Birkelands v 1a, NO-7491 Trondheim, Norway.
[5]Department of Structural Engineering, Norwegian University of Science and Technology
(NTNU), Richard Birkelands v 1a, NO-7491 Trondheim, Norway.

ABSTRACT

Computational Fluid Dynamics (CFD) and Fluid–Structure Interaction (FSI) are growing disciplines in the aeroelastic analysis and design of long-span bridges, which, with their bluff body characteristics, offer major challenges to efficient simulation. In this paper we employ Isogeometric Analysis (IGA) based on Non-Uniform Rational B-Splines (NURBS) to numerically simulate turbulent flows over moving bridge sections in 3D. Stationary and dynamic analyses of two bridge sections, an idealized rectangular shape with aspect ratio 1:10 and a 1:50 scale model of the Hardanger bridge, are performed. Wind tunnel experiments and comparative Finite Element (FE) analyses of the same sections are also conducted. Studies on the convergence, static dependencies on the angle-of-attack, and self-excited forces in terms of the aerodynamic derivatives show that

IGA successfully captures the bluff-body flow characteristics, and exhibits superior per degree-of-freedom accuracy compared to the more traditional lower-order FE discretizations.

INTRODUCTION

The concept of Isogeometric Analysis (IGA) was proposed in (Hughes et al. 2005), in which geometry modeling technologies from Computer-Aided Design (CAD) were applied to the numerical simulation of problems governed by partial differential equations (PDEs). IGA uses Non-Uniform Rational B-Splines (NURBS) (Piegl and Tiller 1995), and other spline types amenable to local refinement, for spatial discretization. NURBS are powerful too for geometry representation and have the advantage of being able to exactly represent all conics. Another important advantage of using NURBS is that the basis functions offer a higher degree of smoothness across element boundaries than standard Finite Element (FE) approximations. A comprehensive introduction to IGA is given in (Cottrell et al. 2009). Since its introduction to structural mechanics, IGA has been successfully applied and proven its efficiency in a large variety of computational physics and engineering areas, such as structural dynamics (Cottrell et al. 2006), contact mechanics (De Lorenzis et al. 2011; Mathisen et al. 2015), Computational Fluid Dynamics (CFD) (Bazilevs et al. 2007a), Fluid–Structure Interaction (FSI) (Bazilevs et al. 2008), including Space-Time (ST) formulations (Takizawa and Tezduyar 2011), phase field modeling (Gómez et al. 2008) and electromagnetics (Buffa et al. 2014), to name a few.

In this paper we combine IGA and the Arbitrary Lagrangian–Eulerian Variational Multiscale (ALE-VMS) formulation for Navier–Stokes equations for incompressible flows (Bazilevs et al. 2012b; Bazilevs et al. 2013a; Bazilevs et al. 2014; Takizawa et al. 2014b; Bazilevs et al. 2015c; Bazilevs et al. 2015b) to simulate bridge aerodynamics. The formulation is augmented with weak enforcement of essential Boundary Conditions (BCs) (Bazilevs et al. 2007b; Bazilevs and Hughes 2007; Bazilevs and Akkerman 2010; Golshan et al. 2015), which alleviate classical restrictions on boundary-layer mesh size, and thus may be thought of as a near-wall model. IGA and VMS methods have been successfully employed, in both ALE and ST context, in a wide range of turbulent flow problems, see, e.g., (Bazilevs et al. 2013a; Hsu et al. 2012; Hsu et al. 2014b; Takizawa et al. 2013a; Yan et al. 2016; Takizawa et al. 2016a; Takizawa et al. 2016b; Takizawa et al. 2017a), including bridge aerodynamics (Scotta et al. 2016). The authors previously applied the ALE-VMS formulation for bridge aerodynamics modeling (Helgedagsrud et al. 2018), but in the context of standard FE for spatial discretizations.

We perform stationary and dynamic simulations for two bridge sections in 3D - an idealized rectangular shape with aspect ratio 1:10 (R10), characterized by the strongly detached flow at the leading edges, and a more streamlined 1:50 scale model of the Hardanger bridge. The former has been studied numerically be several authors, see, e.g., (de Miranda et al. 2014; Patruno 2015). The Hardanger bridge section has been studied previously in (Takizawa et al. 2014a; Helgedagsrud et al. 2017; Helgedagsrud et al. 2018). Numerical simulations of similar generic bridge sections are reported in (Scotta et al. 2016; Larsen and Walther 1998; Bai et al. 2010; Šarkić et al. 2012; Brusiani et al. 2013). Our study focuses on stationary load coefficients and aerodynamic derivatives, which are among the most critical quantities in long-span bridge design. To validate the numerical simulations, forced-vibration wind tunnel experiments were also performed, some of which are reported in (Siedziako et al. 2017; Helgedagsrud et al. 2018), and others carried out specifically for this work.

The bridge deck is taken as a rigid object, and the problem domain is represented by an extruded slice of the wind-tunnel interior with the sectional model installed. NURBS models of the bridge sections are constructed by first defining the initial, coarse multi-patch geometry, and then performing k-refinement to reach quadratic order in all parametric directions. This procedure results in a mostly C^1-continuous discretization with a few C^0 lines.

The paper is outlined as follows. First, the governing equations are presented. Next, we give a brief introduction to NURBS-based IGA followed by a description of the experimental setup and aerodynamic forces. Next, the analysis setup and mesh definition are presented before the numerical results. Lastly, conclusions are drawn.

ALE-VMS FORMULATION OF THE NAVIER–STOKES EQUATIONS OF INCOMPRESSIBLE FLOWS

In this section we summarize the governing equations of the ALE-VMS formulation of incompressible flows. For a thorough description the reader is referred to (Bazilevs et al. 2013a) and references therein.

Governing equations

On a spatial fluid mechanics domain $\Omega_t \in \mathbb{R}^{n_{sd}}$, $n_{sd} = 2, 3$ with boundary Γ_t, with subscript t indicating time-dependence, the Navier–Stokes equations of incompressible flows in the ALE frame may be written as

$$\rho \left(\left.\frac{\partial \mathbf{u}}{\partial t}\right|_{\hat{x}} + (\mathbf{u} - \hat{\mathbf{u}}) \cdot \nabla \mathbf{u} - \mathbf{f} \right) - \nabla \cdot \boldsymbol{\sigma} = 0, \tag{1}$$

$$\nabla \cdot \mathbf{u} = 0. \tag{2}$$

In Eqs. (1)–(2), ρ is the density, $\mathbf{u}$ is the fluid velocity, $\hat{\mathbf{u}}$ is the fluid-domain velocity arising from the ALE description (Hughes et al. 1981), and $\mathbf{f}$ is the body force. The subscript $|_{\hat{x}}$ on the partial derivative denotes that the time-derivative is taken with the referential coordinates $\hat{\mathbf{x}}$ kept fixed. The spatial derivatives are taken with respect to the current position $\mathbf{x}$. $\boldsymbol{\sigma}$ is the fluid Cauchy stress tensor, given by

$$\boldsymbol{\sigma}(\mathbf{u}, p) = -p\mathbf{I} + 2\mu\, \boldsymbol{\varepsilon}(\mathbf{u}), \tag{3}$$

where p and μ are the fluid pressure and dynamic viscosity, respectively, and $\boldsymbol{\varepsilon}(\mathbf{u})$ is the symmetric gradient of $\mathbf{u}$.

Discrete formulation

At the discrete level we partition the fluid domain Ω_t into n_{el} elements denoted Ω_t^e, and the boundary Γ_t into n_{eb} surface elements denoted Γ_t^b, and define the finite-dimensional functional spaces for velocity, pressure and displacement (denoted by $\hat{\mathbf{y}}$), respectively, as $\mathcal{S}_u^h$, $\mathcal{S}_p^h$ and $\mathcal{S}_m^h$, and their corresponding test functions as $\mathcal{V}_u^h$, $\mathcal{V}_p^h$ and $\mathcal{V}_m^h$. Superscript h indicates that its attribute is finite-dimensional. The semi-discrete ALE-VMS formulation is given as follows. Find $\mathbf{u}^h \in \mathcal{S}_u^h$, $p^h \in \mathcal{S}_p^h$ and $\hat{\mathbf{y}}^h \in \mathcal{S}_m^h$, such that $\forall\, \mathbf{w}^h \in \mathcal{V}_u^h$, $q^h \in \mathcal{V}_p^h$ and $\mathbf{w}_m^h \in \mathcal{V}_m^h$:

$$
\begin{aligned}
&\int_{\Omega_t} \mathbf{w}^h \cdot \rho \left(\left.\frac{\partial \mathbf{u}^h}{\partial t}\right|_{\hat{x}} + \left(\mathbf{u}^h - \hat{\mathbf{u}}^h\right) \cdot \boldsymbol{\nabla} \mathbf{u}^h \right) \mathrm{d}\Omega \\
&+ \int_{\Omega_t} \boldsymbol{\varepsilon}(\mathbf{w}^h) : \boldsymbol{\sigma}(\mathbf{u}^h, p^h)\, \mathrm{d}\Omega + \int_{\Omega_t} q^h \boldsymbol{\nabla} \cdot \mathbf{u}^h \, \mathrm{d}\Omega \\
&- \int_{\Omega_t} \mathbf{w}^h \cdot \rho\, \mathbf{f}^h \, \mathrm{d}\Omega - \int_{(\Gamma_t)_h} \mathbf{w}^h \cdot \mathbf{h}^h \, \mathrm{d}\Gamma \\
&+ \sum_{e=1}^{n_{el}} \int_{\Omega_t^e} \tau_{\mathrm{SUPS}} \left(\left(\mathbf{u}^h - \hat{\mathbf{u}}^h\right) \cdot \boldsymbol{\nabla} \mathbf{w}^h + \frac{\boldsymbol{\nabla} q^h}{\rho} \right) \cdot \mathbf{r}_M \left(\mathbf{u}^h, p^h\right) \, \mathrm{d}\Omega \\
&+ \sum_{e=1}^{n_{el}} \int_{\Omega_t^e} \rho \nu_{\mathrm{LSIC}} \boldsymbol{\nabla} \cdot \mathbf{w}^h \mathrm{r}_C(\mathbf{u}^h) \, \mathrm{d}\Omega \\
&- \sum_{e=1}^{n_{el}} \int_{\Omega_t^e} \tau_{\mathrm{SUPS}} \mathbf{w}^h \cdot \left(\mathbf{r}_M \left(\mathbf{u}^h, p^h\right) \cdot \boldsymbol{\nabla} \mathbf{u}^h \right) \, \mathrm{d}\Omega \\
&- \sum_{e=1}^{n_{el}} \int_{\Omega_t^e} \frac{\boldsymbol{\nabla} \mathbf{w}^h}{\rho} : \left(\tau_{\mathrm{SUPS}} \mathbf{r}_M \left(\mathbf{u}^h, p^h\right) \right) \otimes \left(\tau_{\mathrm{SUPS}} \mathbf{r}_M \left(\mathbf{u}^h, p^h\right) \right) \, \mathrm{d}\Omega \\
&+ \int_{\Omega_{\tilde{t}}} \boldsymbol{\varepsilon}(\mathbf{w}_m^h) : \mathbf{D}^h \, \boldsymbol{\varepsilon} \left(\hat{\mathbf{y}}^h(t) - \hat{\mathbf{y}}^h(\tilde{t}) \right) = 0
\end{aligned}
\tag{4}
$$

In Eq. (4), $\mathbf{h}^h$ is the prescribed surface traction. $\mathbf{r}_M$ and r_C are residuals of the Navier–Stokes linear-momentum balance and continuity, respectively, given by

$$
\mathbf{r}_M = \rho \left(\left.\frac{\partial \mathbf{u}^h}{\partial t}\right|_{\hat{x}} + \left(\mathbf{u}^h - \hat{\mathbf{u}}^h\right) \cdot \boldsymbol{\nabla} \mathbf{u}^h - \mathbf{f}^h \right) - \boldsymbol{\nabla} \cdot \boldsymbol{\sigma} \left(\mathbf{u}^h, p^h\right), \tag{5}
$$

$$
\mathrm{r}_C = \boldsymbol{\nabla} \cdot \mathbf{u}^h. \tag{6}
$$

Eq. (4) introduces the stabilization parameters τ_{SUPS} and ν_{LSIC}. These have been designed to render optimal stability and convergence through extensive studies, see e.g., (Hughes et al. 1986; Tezduyar and Park 1986; Tezduyar and Osawa 2000; Tezduyar 2003; Hughes and Sangalli 2007; Hsu et al. 2010; Takizawa et al. 2018) and references therein. In this work we use the definitions given in

(Bazilevs et al. 2008). The last line in Eq. (4) corresponds to the linear elastostatics operator with the elastic tensor $\mathbf{D}^h$, which is used to compute the displacement of the fluid-mechanics mesh interior from the that of the fluid-object interface. In a forced-vibration setting, the fluid-object interface motion is user-defined and is assumed known.

To augment the formulation with weak enforcement of the essential boundary conditions $(\Gamma_t)_g$, they are removed from the trial functions and replaced by the following terms added to the left-hand side of Eq. (4):

$$\begin{aligned}
&-\sum_{b=1}^{n_{eb}} \int_{\Gamma_t^b \cap (\Gamma_t)_g} \mathbf{w}^h \cdot \boldsymbol{\sigma}\left(\mathbf{u}^h, p^h\right) \mathbf{n} \, \mathrm{d}\Gamma \\
&-\sum_{b=1}^{n_{eb}} \int_{\Gamma_t^b \cap (\Gamma_t)_g} \left(2\mu \boldsymbol{\varepsilon}\left(\mathbf{w}^h\right) \mathbf{n} + q^h \mathbf{n}\right) \cdot \left(\mathbf{u}^h - \mathbf{g}^h\right) \, \mathrm{d}\Gamma \\
&-\sum_{b=1}^{n_{eb}} \int_{\Gamma_t^b \cap (\Gamma_t)_g^-} \mathbf{w}^h \cdot \rho \left(\left(\mathbf{u}^h - \hat{\mathbf{u}}^h\right) \cdot \mathbf{n}\right) \left(\mathbf{u}^h - \mathbf{g}^h\right) \, \mathrm{d}\Gamma \\
&+\sum_{b=1}^{n_{eb}} \int_{\Gamma_t^b \cap (\Gamma_t)_g} \tau_{\mathrm{TAN}} \left(\mathbf{w}^h - \left(\mathbf{w}^h \cdot \mathbf{n}\right) \mathbf{n}\right) \cdot \left(\left(\mathbf{u}^h - \mathbf{g}^h\right) \left(\left(\mathbf{u}^h - \mathbf{g}^h\right) \cdot \mathbf{n}\right) \mathbf{n}\right) \, \mathrm{d}\Gamma \\
&+\sum_{b=1}^{n_{eb}} \int_{\Gamma_t^b \cap (\Gamma_t)_g} \tau_{\mathrm{NOR}} \left(\mathbf{w}^h \cdot \mathbf{n}\right) \left(\left(\mathbf{u}^h - \mathbf{g}^h\right) \cdot \mathbf{n}\right) \, \mathrm{d}\Gamma,
\end{aligned} \tag{7}$$

where $\mathbf{n}$ is the outward normal vector of the boundary. τ_{TAN} and τ_{NOR} are boundary penalty parameters in the tangential and normal directions, respectively, as defined in (Bazilevs et al. 2007b), and $(\Gamma_t)_g^-$ is defined as the inflow part of $(\Gamma_t)_g$:

$$(\Gamma_t)_g^- = \left\{ \mathbf{x} | \left(\mathbf{u}^h - \hat{\mathbf{u}}^h\right) \cdot \mathbf{n} < 0, \forall \mathbf{x} \subset (\Gamma_t)_g \right\}. \tag{8}$$

ISOGEOMETRIC ANALYSIS

For space discretization of the ALE-VMS equations we employ NURBS-based IGA. The concept of IGA was proposed in (Hughes et al. 2005) to better integrate CAD and FE. NURBS are the most popular basis-function technology implemented in IGA, where they are used to simultaneously model geometry and provide interpolation spaces for analysis. Similar to FE methods, IGA mostly uses a variational framework, in combination with the isoparametric concept and $p-$ and $h-$refinement, to discretize PDE systems. Attributes that are unique to IGA include higher-order inter-element continuity and a feature called $k-$refinement, where the order and degree of smoothness of the basis functions are raised simultaneously. (See Fig. 1 for an illustration in 1D.)

IGA was first applied in the context of turbulent flows and VMS methods in (Bazilevs et al. 2007a), where it showed excellent performance on a set of challenging benchmark problems. For incompressible turbulent flows, significant improvement in the per-degree-of-freedom accuracy due to the higher-order smoothness of NURBS was clearly demonstrated in (Akkerman et al. 2008; Motlagh and Ahn 2012). NURBS-based IGA in combination with weakly-enforced essential boundary conditions was shown to preform very well for wall-bounded turbulent flows in (Bazilevs et al. 2010) and (Bazilevs and Akkerman 2010). Recent applications of IGA in fluids and FSI include wind-turbine aerodynamics (Hsu et al. 2011; Bazilevs et al. 2013b; Takizawa et al. 2015; Bazilevs et al. 2012a), spacecraft aerodynamics (Takizawa et al. 2013b), cardiovascular fluid mechanics (Bazilevs et al. 2008; Bazilevs et al. 2009; Takizawa et al. 2017c), turbomachinery (Takizawa et al. 2017a) and tire aerodynamics (Takizawa et al. 2018).

Despite the excellent accuracy of NURBS-based discretizations for turbulent flows, IGA still remains a more popular technology for structures, or the “structure part” of the FSI problem (see, e.g., (Bazilevs et al. 2012b; Takizawa et al. 2012; Korobenko et al. 2013; Bazilevs et al. 2013a)). This is due to the fact that many applications make use of shell structures, which may be discretized using surface spline technology that is implemented in many general-purpose geometry modeling and CAD software tools. Volumetric meshing, which is essential for flow problems, is much less developed in IGA, and often requires the use of in-house research codes. However, recent developments in non-matching discretizations and sliding interfaces for CFD (Bazilevs et al. 2012a; Hsu et al. 2014a; Bazilevs et al. 2015a; Takizawa et al. 2017b; Otoguro et al. 2017) are now providing technology to begin eliminating the limitations associated with conforming multi-patch discretizations.

WIND TUNNEL EXPERIMENTS AND AERODYNAMIC FORCES

This section gives a brief presentation of the experimental setup and the definition of aerodynamic forces. The wind tunnel experiments are carried out at the Fluid Mechanics Laboratory of the Norwegian University of Science and Technology using the same setup as in (Siedziako et al. 2017), in which a comprehensive description of the experiments is given. This closed, medium-sized wind tunnel has a 11 m long test section and a cross-sectional dimension of 2.7 m by 1.8 m. Fig. 2 shows the interior of the wind tunnel with the Hardanger bridge sectional model installed. The sectional model is mounted to a six-axis force/torque transducer at each end, which in turn is mounted to a 3 degree-of-freedom actuator driven by electric motors in a user-defined motion.

Since the force measurements include inertia, each motion history needs to be conducted also in still-air. The aerodynamic forces are then given by the difference between the in-wind and still-wind force measurements. This subtraction also cancels out any biasing. The wind velocity is sampled through an upwind pitot tube. The experiments are conducted for wind velocities between 4 and 12 m/s. In this range the turbulence intensity is typically less than 0.2 %.

With reference to the bridge sections and sign convention in Fig. 3, we define the aerodynamic forces, namely, drag D, lift L, and pitching moment M, per unit chord length acting on the line of centroids as:

$$D = \frac{1}{2}\rho U^2 H C_D(t), \tag{9}$$

$$L = \frac{1}{2}\rho U^2 B C_L(t), \tag{10}$$

$$M = \frac{1}{2}\rho U^2 B^2 C_M(t), \tag{11}$$

where U is the mean wind velocity and B and H are the stream-wise and cross-wind dimensions of the cross section, respectively. $C_D(t)$, $C_L(t)$ and $C_M(t)$ are the dimensionless aerodynamic coefficients, typically depending on the geometry and angle of attack.

The motion-induced, or self-excited, contributions of the aerodynamic forces can be expressed using the empirical formulation as originally proposed in (Scanlan and Tomko 1971):

$$C_L^{se}(t) = KH_1^*\frac{\dot{h}}{U} + KH_2^*\frac{B\dot{\theta}}{U} + K^2H_3^*\theta + K^2H_4^*\frac{h}{B}, \tag{12}$$

$$C_M^{se}(t) = KA_1^*\frac{\dot{h}}{U} + KA_2^*\frac{B\dot{\theta}}{U} + K^2A_3^*\theta + K^2A_4^*\frac{h}{B}. \tag{13}$$

where h and θ are the vertical and angular displacements, respectively, as shown in Fig. 3. $K = \omega B/U$ is the so-called reduced frequency, where ω is the circular frequency of the structural motion. H_i^* and A_i^*, $i = \{1 \mathinner{..} 4\}$ are the aerodynamic derivatives. These shape-dependent parameters may be regarded as transfer functions between body motion and self-excited forces, and are commonly expressed as functions of the reduced frequency, K. Superscript se refers to the self-excited part of the forces. See (Chen and Kareem 2002) for more details.

Using the forced-vibration method, whether in the context of experiments or numerical studies, greatly simplifies identification of the aerodynamic derivatives compared to the free-vibration approach. In the simulations, no FSI or fluid-object interaction coupling needs to be considered, because the interface motion is prescribed analytically. In addition, much shorter simulation times are needed to collect the required data for parameter identification. These advantages were pointed out by other authors (see, e.g., (Le Maître et al. 2003; Nieto et al. 2015)). In the present work, the aerodynamic derivatives are identified by the least-squares method described in (Siedziako et al. 2017).

GEOMETRY DEFINITION AND ANALYSIS SETUP

The computational domains represents a 0.25 m wide slice of the wind tunnel, where the ceiling and floor are placed 0.930 m and 0.885 m from the cross section centroid, respectively. The inflow surface, with prescribed uniform velocity U, is placed 1.0 m upwind of the centroid, and the zero-traction outflow surface is placed 3.0 m downwind of the centroid. The bridge-deck sectional models, whose cross sections are shown in Fig. 3, are subjected to weakly-enforced no-slip boundary conditions.

For the idealized rectangular shape, two geometries are considered. The first makes use of sharp corners and is composed of five NURBS patches as shown in Fig. 4. Because the pressure singularities at the sharp corners may lead to increased sensitivity of the results to the problem input, we also created an alternative shape with slightly rounded corners. Here, additional NURBS patches are used to replace the sharp corners with exact circular arcs. The curvature radius is set to $H/50$. This setup is outlined in Fig. 5. Although the physical sectional model is built to represent a true rectangular shape, its actual average radius of curvature is estimated to be $H/500$.

The Hardanger bridge geometry is composed by 17 patches, as shown in Fig. 6. The patches are constructed to yield minimal mesh distortion near the bridge deck surface, see Fig. 7. Also for this section we utilize NURBS to represent the circular leading edges exactly.

The air density ρ and the dynamic viscosity μ is set to 1.1835 $\mathrm{kg/m^3}$ and 1.848×10^{-5} $\mathrm{kg/ms}$, respectively. The computational time stepping is chosen such that the maximum Courant number stays below 2.0, typically $5 - 10 \times 10^{-5}$ s.

From the definition of the initial patch geometry, order elevation and knot insertion is easily performed using the algorithms in (Piegl and Tiller 1995). The continuous mesh is created by merging the boundary nodes of the internal patch surfaces, in which the continuity is C^0.

The computations are performed in a parallel environment adopted from (Hsu et al. 2011), where the domain is partitioned into between 128 and 1024 subdomains using METIS (Karypis and Kumar 1998).

NUMERICAL RESULTS

In this section we present the numerical results, focusing on the load coefficients and aerodynamic derivatives. We also look at the pressure coefficient distribution on the R10 bridge deck surface given by $C_p = p/(1/2\rho U^2)$, and the Strouhal number given by $St = f_w H/U$, where f_w is the vortex-shedding frequency. Both experiment and simulations are performed using the inflow air speed of $U = 8$ m/s, giving the Reynolds number $Re = \rho U B/\mu = 2.6 \times 10^5$.

A numerical Buttersworth filter (Rabiner and Gold 1975) with low-pass frequency of 3 Hz is applied to the raw experimental force data in order to remove signal noise and high-frequency vibrations of the sectional model. These issue are discussed in detail in (Siedziako et al. 2017). Such disturbances do not occur in the numerical simulations, and the results are presented without filtering of the computed force data.

Convergence study

A mesh convergence study is performed on the sharp and rounded R10 sections. Three meshes of increasing resolution are employed in the simulations and shown in Fig. 8. For the section with sharp corners, the coarse mesh (labeled M1) has 36.9×10^3 control points, the medium mesh (labeled M2) has 261.4×10^3 control points, and the fine mesh (labeled M3) has $1\,252.4 \times 10^3$ control points. A similar resolution is employed for the section with rounded corners. From the initial patch definition, we use k-refinement to construct C^1-continuous NURBS analysis meshes that are quadratic in all parametric directions. A mesh convergence study is performed with the bridge section kept fixed at $\theta = 2°$. This configuration is chosen for the following reasons: i) The lift and pitching moment are nonzero, and a linear relationship to the angle of attack can be assumed valid; ii) Earlier work (for aspect ratio 1:8) (Patruno 2015; de Miranda et al. 2014) revealed large differences between experimental and simulation results; and iii) The wind tunnel test results have relatively low scatter at this angle of attack.

The mesh refinement study results are presented in Tab. 1 and Figs. 9 and 10. Fig. 9 illustrates the turbulent-flow features by visualizing vorticity magnitude contours on a spanwise cut, while Fig. 10 compares the pressure distribution on the top and bottom surfaces of the deck for both geometries. The coarse meshes do not capture the flow reattachment and shear layer well. The results improve with mesh refinement, as expected. This lack of good resolution on the coarse meshes is reflected in the corresponding pressure distributions, especially on the top surface of the deck (see Fig. 10). While the overall lift and drag forces are not as sensitive, the aerodynamic center location is shifted, resulting in higher sensitivity of the pitching moment to mesh resolution. Since the pressure distribution reflects the position of flow reattachment, it follows that the pitching moment is mainly governed by the reattachment length. We believe this explains the two-sided convergence of the pitching moment, considering that the reattachment first become more distinct for M2.

The geometry with rounded corners produces a slightly lower drag force, but otherwise very similar results are attained, including response under mesh refinement. The lower drag force mainly results from the fact that the corners render more low-profiled shear layers. This also leads to an earlier reattachment, as can be seen from the pressure distribution, which in this case appear to increase the magnitude of the pitching moment.

Lastly, we note that the top and bottom surface pressure distributions exhibit more consistent convergence patterns for the case of rounded corners. Although rounding the corners is advantageous from the standpoint of numerical stability and convergence, the differences observed in the quantities of interest are not significant to justify using rounded corners in the remaining simulations.

R10 section stationary analysis

We now keep the mesh density fixed at the level of M2, and compute the mean aerodynamic load coefficients with respect to the angle of attack in the range of $\theta = [-5°, 5°]$ for the R10 section with sharp corners. To determine the static coefficients experimentally, we have tested three angle-of-attack time series shown in Fig. 11. The results from the sine wave and fine-resolution staircase are presented as continuous curves, while the coarse staircase is represented by points with temporal statistics.

Stationary simulations are performed in a similar fashion, using the mesh-moving method to construct a similar staircase function. On each interval the simulation is run for 1.5 s of which the last 1 s is sampled. The load coefficients are then represented by their mean value and the 90 % confidence interval of the fluctuation.

For comparison, ALE-VMS FE simulations using linear tetrahedra and approximately the same number of degrees-of-freedom are performed. A thorough description of the FE analysis setup is given in (Helgedagsrud et al. 2018).

Figs. 12, 13 and 14 show the experimentally measured and numerically computed load coefficients for drag, lift and pitching moment, respectively. For drag and lift we are able to capture the absolute value and initial slope with very good accuracy. For the pitching moment, however, the numerical simulations deviate more from the experimental data. As discussed in the convergence study, the pitching moment for this section is extremely sensitive to the reattachment length. In the FE simulation the flow stays detached much longer, which consequently leads to a smaller magnitude of the pitching moment. This leads again to a premature appearance of the non-linear behavior that occurs at the angle-of-attack when the flow does not attack at all. The same non-linear features are also seen for the lifting force, however less prominent. In this respect IGA shows good agreement with the experiments. Earlier works analyzing the same section (de Miranda et al. 2014; Patruno 2015) also point out the difficulties and sensitivity of the pitching moment.

Although FE captures the initial slope of the pitching moment better, we claim that we are able to achieve an overall better per-degree-of-freedom accuracy with IGA, when we take drag and lift and the point of no reattachment into account. Finally, we would like to point out that, especially for the pitching moment, the experiments must be taken with some uncertainty. Due to the large ratio between the lift and pitching moment, small disturbances such as vibration of the sectional model, geometrical imperfections and free-stream turbulence (Mills et al. 2002) may give a significant impact on the latter.

Hardanger section stationary analysis

Stationary analyses are performed for the Hardanger bridge section using the same simulation strategy. A similar mesh density is used as in the quadratic NURBS model for the R10 deck, giving a total of 313×10^3 control points. Figs. 15, 16 and 17 show the load coefficients for drag, lift and pitching moment, respectively. For this bridge section we capture the slope of the lift and pitching moment curves with excellent accuracy, however, the absolute values are slightly shifted. For the drag, the simulations show less sensitivity to the angle of attack than is observed in the experiments. Unlike for the R10 section, IGA does not show as much improvement over FE. Nevertheless, IGA gives better per degree-of-freedom accuracy for: i) Absolute value of the drag; and ii) Slopes of the lift and pitching-moment curves. The latter is important for the computation of aerodynamic derivatives, as the stationary analyses represent the limit of $U_{red} \rightarrow \infty$.

Compared to the R10 section, the Hardanger section exhibits a much more streamlined behavior, and the flow stays mostly attached, even for large pitching angles, as can be seen from the velocity contours shown in Fig. 18. This explains the less pronounced differences between IGA and FE simulations, considered that variation in the reattachment length appeared in the previous sections to be a major source of uncertainty. Although the flow is mostly attached, small differences in the flow separations that occur at the top and bottom surface toward the leading edge and the fact that the section is unsymmetrical in height may further explain the differences in the absolute value of the lift and pitching moment. E.g., a small increase in the reattachment length on the bottom surface will increase the base suction at the lower upwind corner, which again will lead to a decrease in the lift and the pitching moment, as seen in Figs. 16 and 17.

Forced-vibration analysis and aerodynamic derivatives

We now actuate the R10 and Hardanger bridge decks in the torsional and vertical harmonic motion in order to carry our forced-vibration experiments and simulations, and compute aerodynamic derivatives. An overview of the test conditions for the wind tunnel experiments and numerical simulations is given in Tab. 2. Different vibration frequencies, run sequentially, and different wind velocities (for the experiments only) are analyzed in order to obtain the dependence of the aerodynamic derivatives on the reduced frequency K. A thorough description of the experimental setup is reported in (Siedziako et al. 2017), where the identification procedure for the aerodynamic derivatives is also described. A comprehensive description of the numerical approach for the forced-vibration simulations, including the mesh-moving algorithms, is given in (Helgedagsrud et al. 2018), where aerodynamic derivatives for the same sections were computed using tetrahedral FE. For comparison, the results from that reference are presented alongside the IGA results from the present analysis. We note, however, that the FE computations used approximately twice the number of degrees-of-freedom compared to the IGA models.

The bridge sections are initially kept at rest for 1 s in order to develop the flow prior to starting the moving-domain forced-vibration simulations. To ensure that the self-excited forces can be regarded as a stationary process, the first 0.25 s of data after the sections are set in motion are ignored. The self-excited forces are then sampled over two complete cycles. Figs. 19 and 20 show examples of the forced-vibration time series, more specifically the R10 section undergoing vertical and torsional motions, respectively, at the frequency of $f = 0.8$ Hz. In the same plots the predicted aerodynamic forces, back-substituted from Eqs. (12) and (13) and the aerodynamic derivatives (labeled IGA AD) and the experimentally obtained self-excited forces are shown.

The aerodynamic derivatives for the R10 section are shown in Fig. 21 We observe that the H^*-type aerodynamic derivatives that govern the self-excited lift force are captured with very good accuracy, and IGA outperforms FE both in terms of magnitudes and phase angles. The A^*-type aerodynamic derivatives, however, are overestimated in the simulations. This also corresponds with the steep inclination seen in Fig. 14. Regarding the phase angle of the self-excited pitching moments, IGA produce more accurate results than the FE simulations. The overestimated pitching moments will consequently lead to a reduction of the critical wind speed compared with the wind tunnel experiments.

The aerodynamic derivatives for the Hardanger section are shown in Fig. 22. Consistent with the findings in the stationary analysis, IGA is in better agreement than FE with the experimental data, especially for the most important aerodynamic derivatives in flutter analysis, H_3^*, A_1^*, A_2^* and A_3^* (Øiseth et al. 2010). Similar to the R10 section, IGA overestimate the lifting forces to a lesser extent than FE, however, the differences between the two approaches are not as pronounced.

CONCLUSIONS

In this work we investigated the application NURBS-based IGA to the simulation of bluff body aerodynamics on moving domains with emphasis on bridge engineering. IGA shares many features with the more standard FE analysis, but also possesses unique features, such as exact geometry and higher-order smoothness that have proven beneficial in many applications, including turbulent flows (Motlagh and Ahn 2012; Bazilevs and Akkerman 2010; Hsu et al. 2011).

The present study considered a rectangular section with aspect ratio $B/H = 10$ (R10) and a 1:50 scale sectional model of the Hardanger bridge. To validate and assess the accuracy and efficiency of the IGA approach, wind tunnel experiments were conducted for the same sections, and FE analyses were carried out for comparison purposes.

A mesh convergence study on a stationary R10 shape at 2° angle of attack were performed. Geometries with sharp and slightly rounded corners were considered. The geometry with rounded corners produced a more consistent convergence pattern for the load coefficients and pressure distribution, and resulted in slightly lower drag values. The moment coefficient exhibited the most deviation from experimental values, which confirms the findings by other researchers (de Miranda et al. 2014; Patruno 2015). This example is, in part, meant to illustrate the challenges of simulating turbulent flows over bluff bodies for bridge aerodynamics.

The aerodynamic load coefficients for the R10 and Hardanger sections were computed from stationary analyses at angles of attack in the range of $[-5°, 5°]$. Comparative wind tunnel experiments and FE analyses show that IGA was able to capture the aerodynamic forces with very good accuracy, and generally outperformed the FE approach. IGA showed significant improvement for the more challenging R10 shape. For the Hardanger bridge section, a more modest improvement over FE of the slopes of the lift and pitching-moment curves were obtained using IGA. In general, both methods performed very well for this more streamlined section.

The IGA approach was employed for moving-domain forced-vibration simulations, and the aerodynamic derivatives were computed for both bridge sections. The self-excited forces were captured with good accuracy, especially for the R10 section, where, as in the prior simulations, IGA showed a significant improvement over FE.

The investigations presented herein have shown that IGA, in combination with the ALE-VMS technique and weakly enforced essential BCs, presents a powerful tool for the simulation of bridge aerodynamics on moving domains. The validity of the proposed approach was strengthened by comparing the IGA simulations with experimental measurements and more standard FE simulations. We also find it counterintuitive (and somewhat ironic) that it is the geometrically simpler shapes that appear to be more challenging for simulating bluff-body turbulent arodynamics than complex-geometry objects.

ACKNOWLEDGMENTS

This work was carried out with financial support from the Norwegian Public Roads Administration. All simulations were performed on resources provided by UNINETT Sigma2 - the National Infrastructure for High Performance Computing and Data Storage in Norway. The authors greatly acknowledge this support.

REFERENCES

Akkerman, I., Bazilevs, Y., Calo, V. M., Hughes, T. J. R., and Hulshoff, S. (2008). "The role of continuity in residual-based variational multiscale modeling of turbulence." *Computational Mechanics*, 41(3), 371–378.

Bai, Y., Sun, D., and Lin, J. (2010). "Three dimensional numerical simulations of long-span bridge aerodynamics, using block-iterative coupling and DES." *Computers and Fluids*, 39(9), 1549–1561.

Bazilevs, Y. and Akkerman, I. (2010). "Large eddy simulation of turbulent Taylor-Couette flow using isogeometric analysis and the residual-based variational multiscale method." *Journal of Computational Physics*, 229(9), 3402–3414.

Bazilevs, Y., Calo, V., Cottrell, J., Hughes, T., Reali, A., and Scovazzi, G. (2007a). "Variational multiscale residual-based turbulence modeling for large eddy simulation of incompressible flows." *Computer Methods in Applied Mechanics and Engineering*, 197(1-4), 173–201.

Bazilevs, Y., Calo, V. M., Hughes, T. J. R., and Zhang, Y. (2008). "Isogeometric fluid-structure interaction: Theory, algorithms, and computations." *Computational Mechanics*, 43(1), 3–37.

Bazilevs, Y., Gohean, J. R., Hughes, T. J. R., Moser, R. D., and Zhang, Y. (2009). "Patient-specific isogeometric fluid-structure interaction analysis of thoracic aortic blood flow due to implantation of the Jarvik 2000 left ventricular assist device." *Computer Methods in Applied Mechanics and Engineering*, 198(45-46), 3534–3550.

Bazilevs, Y., Hsu, M.-C., and Scott, M. (2012a). "Isogeometric fluid–structure interaction analysis with emphasis on non-matching discretizations, and with application to wind turbines." *Computer Methods in Applied Mechanics and Engineering*, 249-252, 28–41.

Bazilevs, Y., Hsu, M.-C., Takizawa, K., and Tezduyar, T. E. (2012b). "ALE-VMS and ST-VMS methods for computer modeling of wind-turbine rotor aerodynamics and fluid-structure interaction." *Mathematical Models and Methods in Applied Sciences*, 22(supp02), 1230002.

Bazilevs, Y. and Hughes, T. J. R. (2007). "Weak imposition of Dirichlet boundary conditions in fluid mechanics." *Computers and Fluids*, 36(1), 12–26.

Bazilevs, Y., Korobenko, A., Deng, X., and Yan, J. (2015a). "Novel structural modeling and mesh moving techniques for advanced fluid-structure interaction simulation of wind turbines." *International Journal for Numerical Methods in Engineering*, 102(3-4), 766–783.

Bazilevs, Y., Korobenko, A., Yan, J., Pal, A., Gohari, S. M. I., and Sarkar, S. (2015b). "ALE–VMS formulation for stratified turbulent incompressible flows with applications." *Mathematical Models and Methods in Applied Sciences*, 25(12), 2349–2375.

Bazilevs, Y., Michler, C., Calo, V., and Hughes, T. (2010). "Isogeometric variational multiscale modeling of wall-bounded turbulent flows with weakly enforced boundary conditions on unstretched meshes." *Computer Methods in Applied Mechanics and Engineering*, 199(13-16), 780–790.

Bazilevs, Y., Michler, C., Calo, V. M., and Hughes, T. J. R. (2007b). "Weak Dirichlet boundary conditions for wall-bounded turbulent flows." *Computer Methods in Applied Mechanics and Engineering*, 196(49-52), 4853–4862.

Bazilevs, Y., Takizawa, K., and Tezduyar, T. E. (2013a). "Challenges and directions in computational fluid-structure interaction." *Mathematical Models and Methods in Applied Sciences*, 23(02), 215–221.

Bazilevs, Y., Takizawa, K., and Tezduyar, T. E. (2013b). *Computational Fluid-Structure Interaction*. John Wiley & Sons, Ltd, Chichester, UK, <http://doi.wiley.com/10.1002/9781118483565> (jan).

Bazilevs, Y., Takizawa, K., and Tezduyar, T. E. (2015c). "New directions and challenging computations in fluid dynamics modeling with stabilized and multiscale methods." *Mathematical Models and Methods in Applied Sciences*, 25(12), 2217–2226.

Bazilevs, Y., Takizawa, K., Tezduyar, T. E., Hsu, M.-C., Kostov, N., and McIntyre, S. (2014). "Aerodynamic and FSI Analysis of Wind Turbines with the ALE-VMS and ST-VMS Methods." *Archives of Computational Methods in Engineering*, 21(4), 359–398.

Brusiani, F., Miranda, S. D., Patruno, L., Ubertini, F., and Vaona, P. (2013). "On the evaluation of bridge deck flutter derivatives using RANS turbulence models." *Journal of Wind Engineering*, 119, 39–47.

Buffa, A., Sangalli, G., and Vázquez, R. (2014). "Isogeometric methods for computational electromagnetics: B-spline and T-spline discretizations." *Journal of Computational Physics*, 257, 1291–1320.

Chen, X. and Kareem, A. (2002). "Advances in Modeling of Aerodynamic Forces on Bridge Decks." *Journal of Engineering Mechanics*, 128(11), 1193–1205.

Cottrell, J., Reali, A., Bazilevs, Y., and Hughes, T. (2006). "Isogeometric analysis of structural vibrations." *Computer Methods in Applied Mechanics and Engineering*, 195(41-43), 5257–5296.

Cottrell, J. A., Hughes, T. J. R., and Bazilevs, Y. (2009). *Isogeometric Analysis*. John Wiley & Sons, Ltd, Chichester, UK, <http://doi.wiley.com/10.1002/9780470749081> (aug).

De Lorenzis, L., Temizer, I., Wriggers, P., and Zavarise, G. (2011). "A large deformation frictional contact formulation using NURBS-based isogeometric analysis." *International Journal for Numerical Methods in Engineering*, 87(13), n/a–n/a.

de Miranda, S., Patruno, L., Ubertini, F., and Vairo, G. (2014). "On the identification of flutter derivatives of bridge decks via RANS turbulence models: Benchmarking on rectangular prisms." *Engineering Structures*, 76, 359–370.

Golshan, R., Tejada-Martínez, A. E., Juha, M., and Bazilevs, Y. (2015). "Large-eddy simulation with near-wall modeling using weakly enforced no-slip boundary conditions." *Computers & Fluids*, 118, 172–181.

Gómez, H., Calo, V. M., Bazilevs, Y., and Hughes, T. J. (2008). "Isogeometric analysis of the Cahn–Hilliard phase-field model." *Computer Methods in Applied Mechanics and Engineering*, 197(49-50), 4333–4352.

Helgedagsrud, T. A., Bazilevs, Y., Korobenko, A., Mathisen, K. M., and Øiseth, O. A. (2018). "Using ALE-VMS to compute aerodynamic derivatives of bridge sections." *Computers & Fluids*.

Helgedagsrud, T. A., Mathisen, K. M., Bazilevs, Y., Øiseth, O., and Korobenko, A. (2017). "Using ALE-VMS to compute wind forces on moving bridge decks." *Proceedings of MekIT'17 Ninth National Conference on Computational Mechanics*, B. Skallerud and H. I. Andersson, eds., Barcelona, Spain, CMIME, 169–189.

Hsu, M. C., Akkerman, I., and Bazilevs, Y. (2011). "High-performance computing of wind turbine aerodynamics using isogeometric analysis." *Computers and Fluids*, 49(1), 93–100.

Hsu, M.-C., Akkerman, I., and Bazilevs, Y. (2012). "Wind turbine aerodynamics using ALE–VMS: validation and the role of weakly enforced boundary conditions." *Computational Mechanics*, 50(4), 499–511.

Hsu, M.-C., Akkerman, I., and Bazilevs, Y. (2014a). "Finite element simulation of wind turbine aerodynamics: validation study using NREL Phase VI experiment." *Wind Energy*, 17(3), 461–481.

Hsu, M.-C., Bazilevs, Y., Calo, V., Tezduyar, T., and Hughes, T. (2010). "Improving stability of stabilized and multiscale formulations in flow simulations at small time steps." *Computer Methods in Applied Mechanics and Engineering*, 199(13-16), 828–840.

Hsu, M.-C., Kamensky, D., Bazilevs, Y., Sacks, M. S., and Hughes, T. J. R. (2014b). "Fluid–structure interaction analysis of bioprosthetic heart valves: significance of arterial wall deformation." *Computational Mechanics*, 54(4), 1055–1071.

Hughes, T. J., Cottrell, J. A., and Bazilevs, Y. (2005). "Isogeometric analysis: CAD, finite elements, NURBS, exact geometry and mesh refinement." *Computer Methods in Applied Mechanics and Engineering*, 194(39-41), 4135–4195.

Hughes, T. J., Franca, L. P., and Balestra, M. (1986). "A new finite element formulation for computational fluid dynamics: V. Circumventing the babuška-brezzi condition: a stable Petrov-Galerkin formulation of the stokes problem accommodating equal-order interpolations." *Computer Methods in Applied Mechanics and Engineering*, 59(1), 85–99.

Hughes, T. J. R., Liu, W. K., and Zimmermann, T. K. (1981). “Lagrangian-Eulerian finite element formulation for incompressible viscous flows.” *Computer Methods in Applied Mechanics and Engineering*, 29(3), 329–349.

Hughes, T. J. R. and Sangalli, G. (2007). “Variational Multiscale Analysis: the Fine scale Green’s Function, Projection, Optimization, Localization, and Stabilized Methods.” *SIAM Journal on Numerical Analysis*, 45(2), 539–557.

Karypis, G. and Kumar, V. (1998). “A Fast and High Quality Multilevel Scheme for Partitioning Irregular Graphs.” *SIAM Journal on Scientific Computing*, 20(1), 359–392.

Korobenko, A., Hsu, M.-C., Akkerman, I., Tippmann, J., and Bazilevs, Y. (2013). “Structural Mechanics Modeling and FSI Simulation of Wind Turbines.” *Mathematical Models and Methods in Applied Sciences*, 23(02), 249–272.

Larsen, A. and Walther, J. H. (1998). “Discrete vortex simulation of flow around five generic bridge deck sections.” *Journal of Wind Engineering and Industrial Aerodynamics*, 77-78, 591–602.

Le Maître, O. P., Scanlan, R. H., and Knio, O. M. (2003). “Estimation of the flutter derivatives of an NACA airfoil by means of Navier-Stokes simulation.” *Journal of Fluids and Structures*, 17(1), 1–28.

Mathisen, K. M., Okstad, K. M., Kvamsdal, T., and Raknes, S. B. (2015). “Simulation of Contact Between Subsea Pipeline and Trawl Gear using Mortar-based Isogeometric Analysis.” *MARINE 2015 - Computational Methods in Marine Engineering VI, Rome, Italy, June 15–17, 2015*, International Center for Numerical Methods in Engineering (CIMNE), 290–305.

Mills, R., Sheridan, J., and Hourigan, K. (2002). “Response of base suction and vortex shedding from rectangular prisms to transverse forcing.” *Journal of Fluid Mechanics*, 461, 25–49.

Motlagh, Y. G. and Ahn, H. T. (2012). “Laminar and turbulent channel flow simulation using residual based variational multi-scale method.” *Journal of Mechanical Science and Technology*, 26(2), 447–454.

Nieto, F., Owen, J. S., Hargreaves, D. M., and Hernández, S. (2015). “Bridge deck flutter derivatives: Efficient numerical evaluation exploiting their interdependence.” *Journal of Wind Engi-*

neering and Industrial Aerodynamics journal, 136, 138–150.

Øiseth, O., Rönnquist, A., and Sigbjörnsson, R. (2010). “Simplified prediction of wind-induced response and stability limit of slender long-span suspension bridges, based on modified quasi-steady theory: A case study.” *Journal of Wind Engineering and Industrial Aerodynamics*, 98(12), 730–741.

Otoguro, Y., Takizawa, K., and Tezduyar, T. E. (2017). “Space–time VMS computational flow analysis with isogeometric discretization and a general-purpose NURBS mesh generation method.” *Computers & Fluids*, 158, 189–200.

Patruno, L. (2015). “Accuracy of numerically evaluated flutter derivatives of bridge deck sections using RANS: Effects on the flutter onset velocity.” *Engineering Structures*, 89, 49–65.

Piegl, L. and Tiller, W. (1995). *The NURBS Book*. Monographs in Visual Communications. Springer Berlin Heidelberg, Berlin, Heidelberg, <http://link.springer.com/10.1007/978-3-642-97385-7>.

Rabiner, L. R. and Gold, B. (1975). *Theory and application of digital signal processing*. Prentice-Hall, Englewood Cliffs, N.J.

Šarkić, A., Fisch, R., Höffer, R., and Bletzinger, K. U. (2012). “Bridge flutter derivatives based on computed, validated pressure fields.” *Journal of Wind Engineering and Industrial Aerodynamics*, 104-106, 141–151.

Scanlan, R. H. and Tomko, J. (1971). “Airfoil and bridge deck flutter derivatives.” *Journal of the Engineering Mechanics Division*, 97(6), 1717–1737.

Scotta, R., Lazzari, M., Stecca, E., Cotela, J., and Rossi, R. (2016). “Numerical wind tunnel for aerodynamic and aeroelastic characterization of bridge deck sections.” *Computers and Structures*, 167, 96–114.

Siedziako, B., Øiseth, O., and Rønnquist, A. (2017). “An enhanced forced vibration rig for wind tunnel testing of bridge deck section models in arbitrary motion.” *Journal of Wind Engineering and Industrial Aerodynamics*, 164(February), 152–163.

Takizawa, K., Bazilevs, Y., Tezduyar, T. E., Hsu, M.-C., Øiseth, O., Mathisen, K. M., Kostov, N., and McIntyre, S. (2014a). “Engineering Analysis and Design with ALE-VMS and Space-Time Methods.” *Archives of Computational Methods in Engineering*, 21(4), 481–508.

Takizawa, K., Bazilevs, Y., Tezduyar, T. E., Long, C. C., Marsden, A. L., and Schjodt, K. (2014b). “ST and ALE-VMS methods for patient-specific cardiovascular fluid mechanics modeling.” *Mathematical Models and Methods in Applied Sciences*, 24(12), 2437–2486.

Takizawa, K., Henicke, B., Puntel, A., Kostov, N., and Tezduyar, T. E. (2012). “Space-time techniques for computational aerodynamics modeling of flapping wings of an actual locust.” *Computational Mechanics*, 50(6), 743–760.

Takizawa, K., Henicke, B., Puntel, A., Kostov, N., and Tezduyar, T. E. (2013a). “Computer modeling techniques for flapping-wing aerodynamics of a locust.” *Computers & Fluids*, 85, 125–134.

Takizawa, K., Montes, D., McIntyre, S., and Tezduyar, T. E. (2013b). “Space-time VMS methods for modeling of incompressible flows at high Reynolds numbers.” *Mathematical Models and Methods in Applied Sciences*, 23(02), 223–248.

Takizawa, K. and Tezduyar, T. E. (2011). “Multiscale space-time fluid-structure interaction techniques.” *Computational Mechanics*, 48(3), 247–267.

Takizawa, K., Tezduyar, T. E., Asada, S., and Kuraishi, T. (2016a). “Space–Time method for flow computations with slip interfaces and topology changes (ST-SI-TC).” *Computers & Fluids*, 141, 124–134.

Takizawa, K., Tezduyar, T. E., and Hattori, H. (2017a). “Computational analysis of flow-driven string dynamics in turbomachinery.” *Computers & Fluids*, 142, 109–117.

Takizawa, K., Tezduyar, T. E., Kuraishi, T., Tabata, S., and Takagi, H. (2016b). “Computational thermo-fluid analysis of a disk brake.” *Computational Mechanics*, 57(6), 965–977.

Takizawa, K., Tezduyar, T. E., Mochizuki, H., Hattori, H., Mei, S., Pan, L., and Montel, K. (2015). “Space–time VMS method for flow computations with slip interfaces (ST-SI).” *Mathematical Models and Methods in Applied Sciences*, 25(12), 2377–2406.

Takizawa, K., Tezduyar, T. E., and Otoguro, Y. (2018). “Stabilization and discontinuity-capturing parameters for space–time flow computations with finite element and isogeometric discretizations." *Computational Mechanics*.

Takizawa, K., Tezduyar, T. E., Otoguro, Y., Terahara, T., Kuraishi, T., and Hattori, H. (2017b). "Turbocharger flow computations with the Space–Time Isogeometric Analysis (ST-IGA)." *Computers and Fluids*, 142, 15–20.

Takizawa, K., Tezduyar, T. E., Terahara, T., and Sasaki, T. (2017c). "Heart valve flow computation with the integrated Space–Time VMS, Slip Interface, Topology Change and Isogeometric Discretization methods." *Computers & Fluids*, 158, 176–188.

Tezduyar, T. and Park, Y. (1986). "Discontinuity-capturing finite element formulations for nonlinear convection-diffusion-reaction equations." *Computer Methods in Applied Mechanics and Engineering*, 59(3), 307–325.

Tezduyar, T. E. (2003). "Computation of moving boundaries and interfaces and stabilization parameters." *International Journal for Numerical Methods in Fluids*, 43(5), 555–575.

Tezduyar, T. E. and Osawa, Y. (2000). "Finite element stabilization parameters computed from element matrices and vectors." *Computer Methods in Applied Mechanics and Engineering*, 190, 411–430.

Yan, J., Korobenko, A., Deng, X., and Bazilevs, Y. (2016). "Computational free-surface fluid–structure interaction with application to floating offshore wind turbines." *Computers & Fluids*, 141, 155–174.

List of Tables

TABLE 1. Averaged load coefficients and Strouhal numbers for mesh refinement study of the R10 bridge section at 2° angle-of-attack and $Re = 2.6 \times 10^5$.

Method	$\bar{C}_D$	$\bar{C}_L$	$\bar{C}_M$	St
Experiment	1.25	0.29	0.030	0.17 – 0.19
M1 sharp	1.23	0.33	0.053	0.17 – 0.19
M2 sharp	1.14	0.33	0.061	0.18 – 0.20
M3 sharp	1.17	0.37	0.053	0.15 – 0.17
M1 rounded	1.14	0.31	0.059	0.22 – 0.23
M2 rounded	1.09	0.33	0.065	0.21 – 0.22
M3 rounded	1.11	0.34	0.060	0.19 – 0.21

TABLE 2. Forced-vibration test setup for wind tunnel experiments and simulations. In the experiments each frequency is run for 50 s, giving rise to a variable number of cycles.

Property	Wind tunnel	Simulations
Amplitude h	15 mm	15 mm
Amplitude θ	2°	2°
Wind velocities	4, 8, 10 and 12 m/s	8 m/s
Vibration frequencies	0.5, 0.8, 1.1, 1.4, 1.7, 2.0 and 2.5 Hz	0.5, 0.8, 1.1 and 2.0 Hz
Number of cycles	25 – 100	2
Sampling frequency	200 Hz	250 Hz

List of Figures

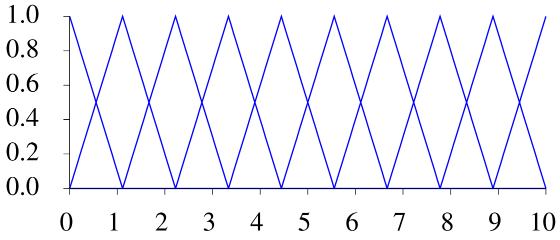

(a) C^0-linear.

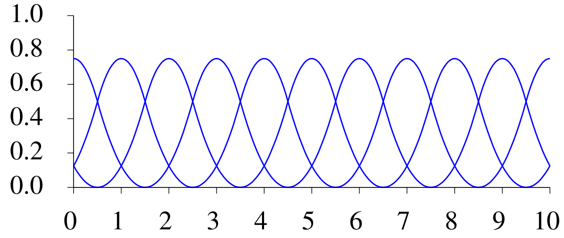

(b) C^1-quadratic.

Fig. 1. One-dimensional basis functions for C^0-linear and C^1-quadratic isogeometric analysis.

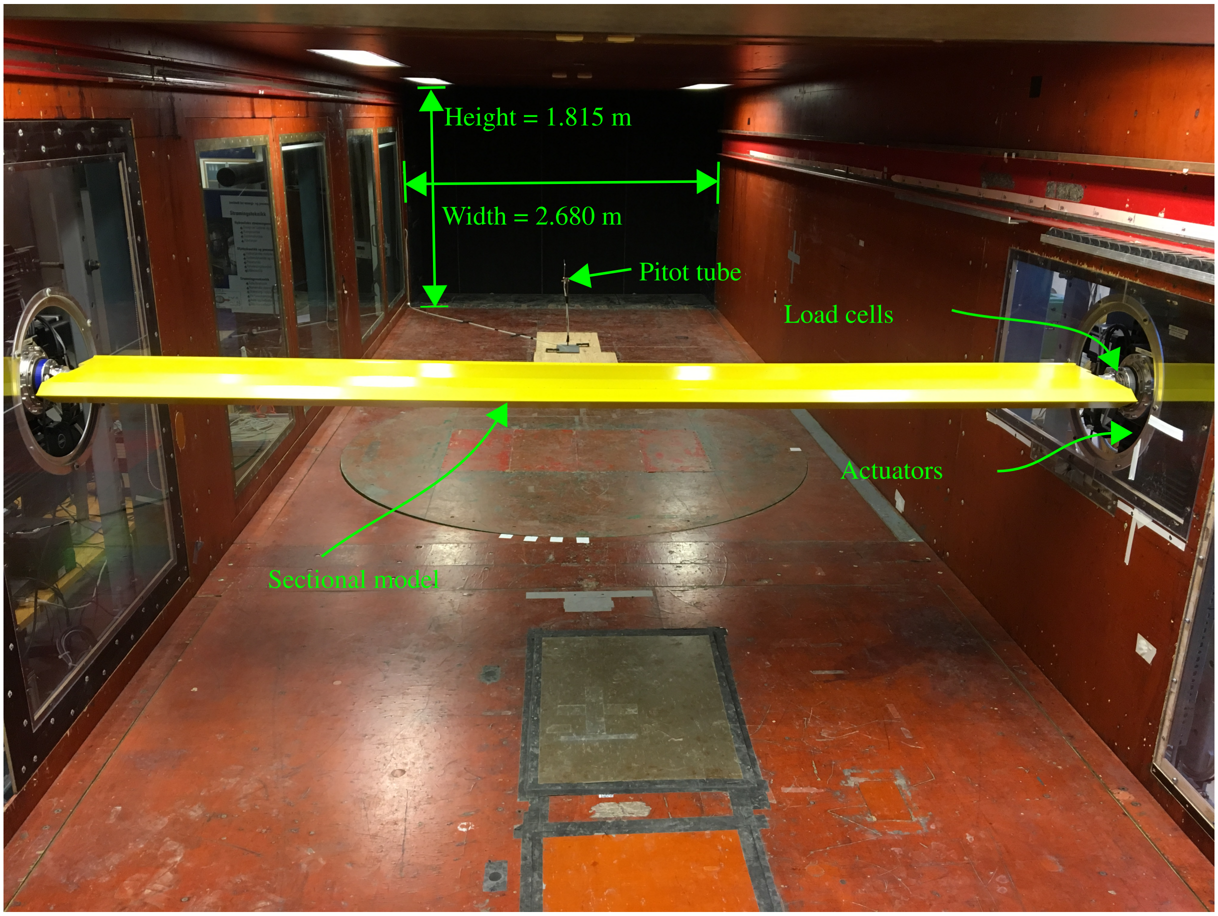

Fig. 2. Inside the wind tunnel with the Hardanger bridge sectional model installed.

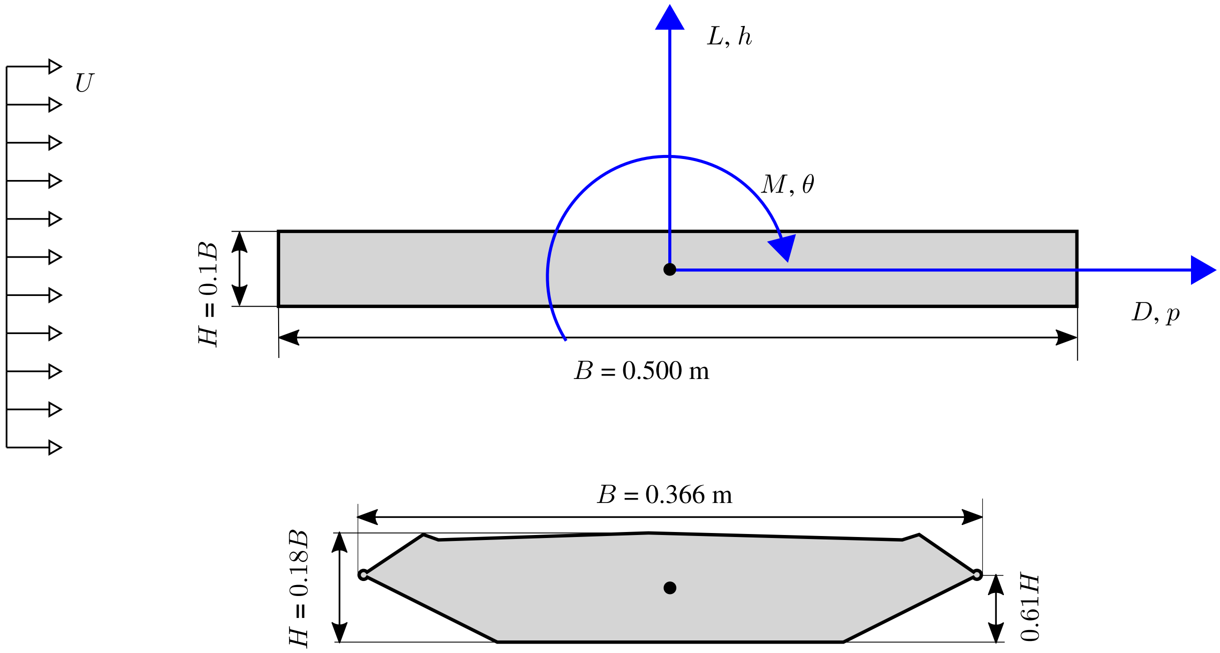

Fig. 3. Geometries of the R10 and Hardanger cross sections with the definition of the aerodynamic forces shown on the former. Note the direction of the pitching moment.

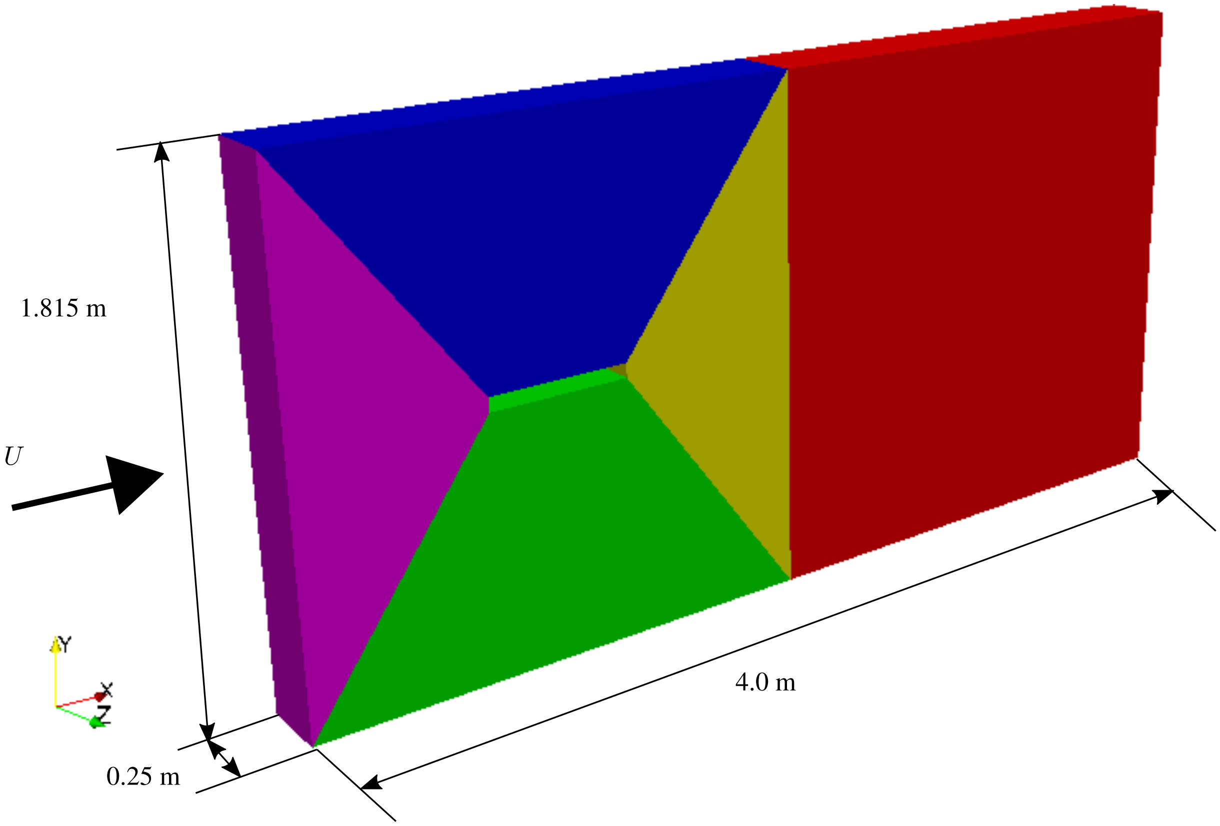

Fig. 4. Computational domain constructed from five NURBS patches representing a slice of the wind tunnel.

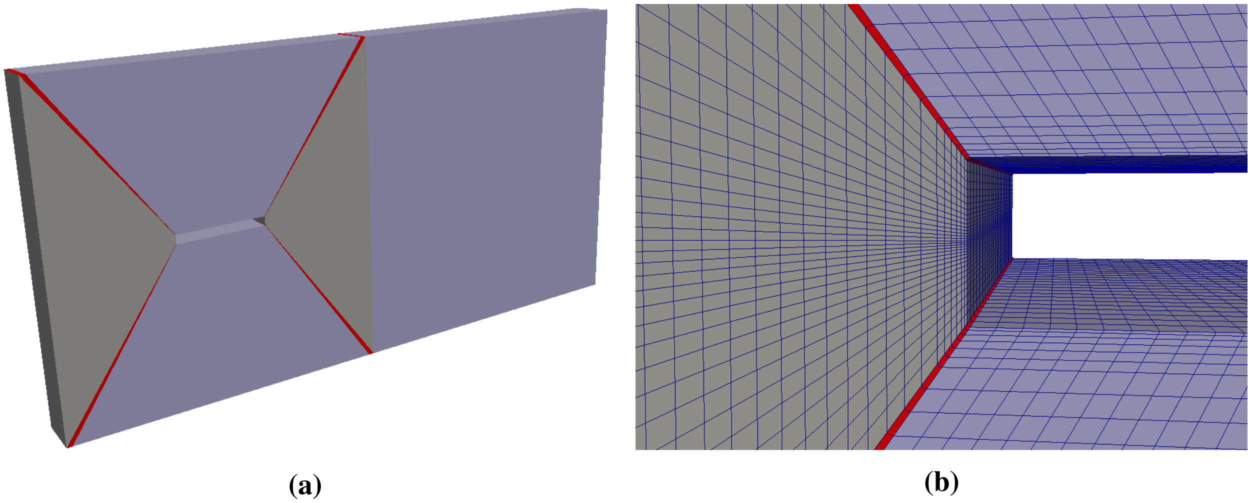

Fig. 5. Nine NURBS patches representing the R10 section with rounded corners: a) Full view; b) Zoom on the leading edge indicating the scale of curvature.

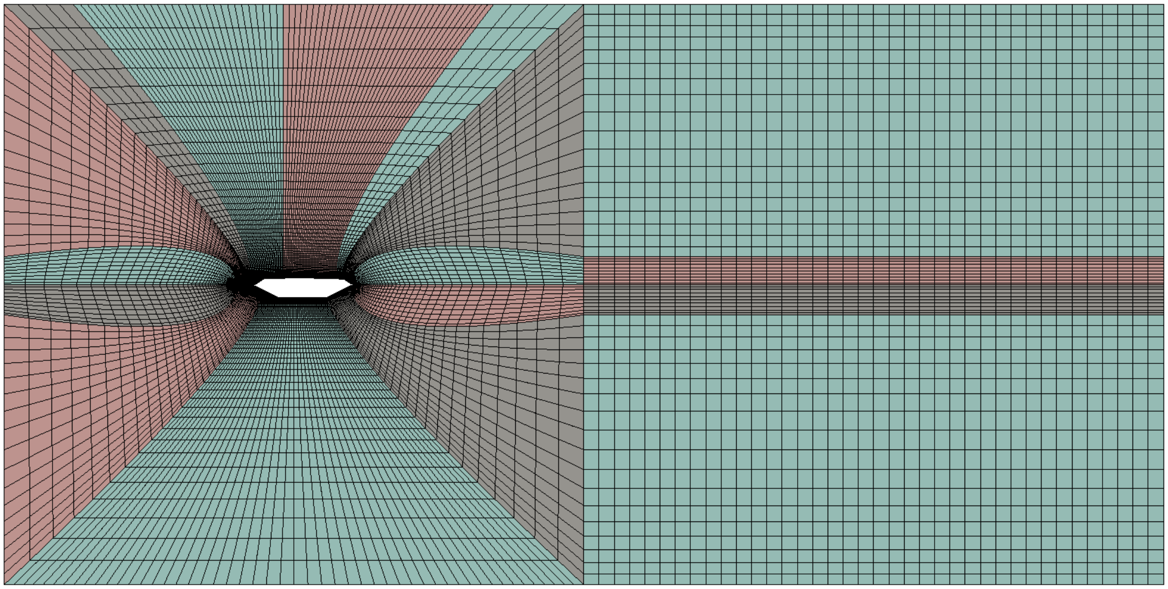

Fig. 6. Patch topology for the Hardanger bridge section.

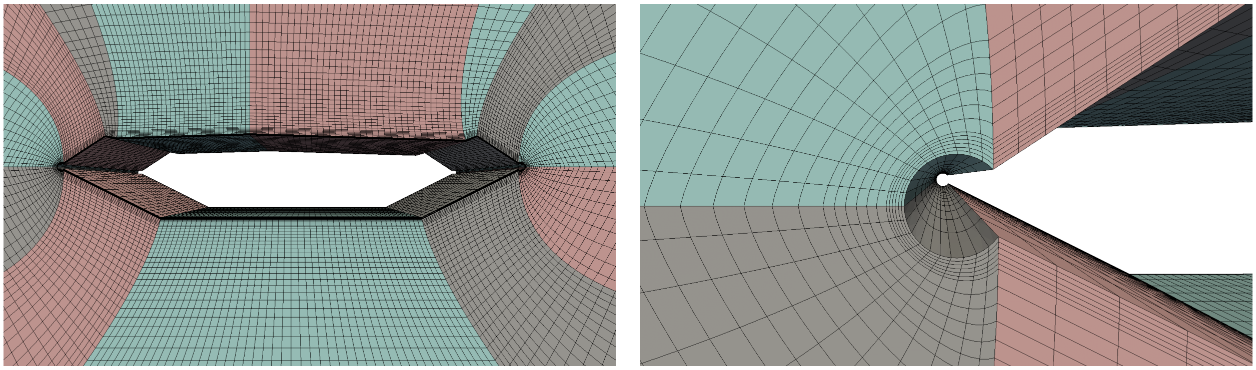

(a) **(b)**

Fig. 7. Analysis model of the Hardanger bridge. a) Zoom on the bridge deck; b) Further zoom on the leading edge.

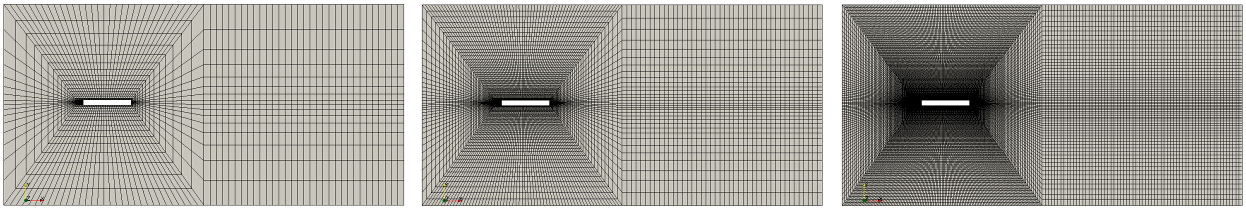

Fig. 8. NURBS meshes used in the convergence study of the R10 section with sharp corners. For visualization purposes, quadratic NURBS elements are interpolated using standard serendipity elements.

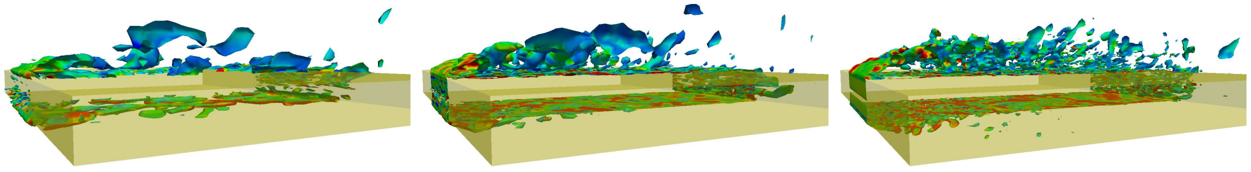

(a) M1 sharp **(b)** M2 sharp **(c)** M3 sharp

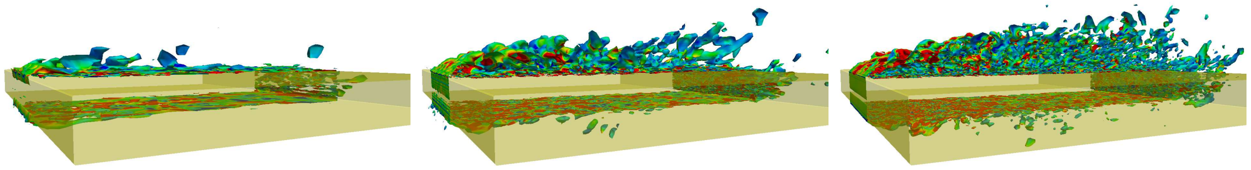

(d) M1 rounded **(e)** M2 rounded **(f)** M3 rounded

Fig. 9. Convergence of the instantaneous vorticity magnitude for the two R10 geometries.

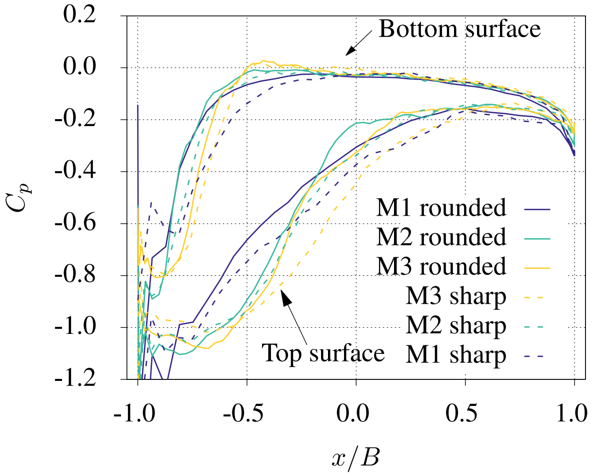

Fig. 10. Pressure distribution on the top and bottom surfaces of the R10 section with sharp and rounded corners. Mesh refinement results are plotted.

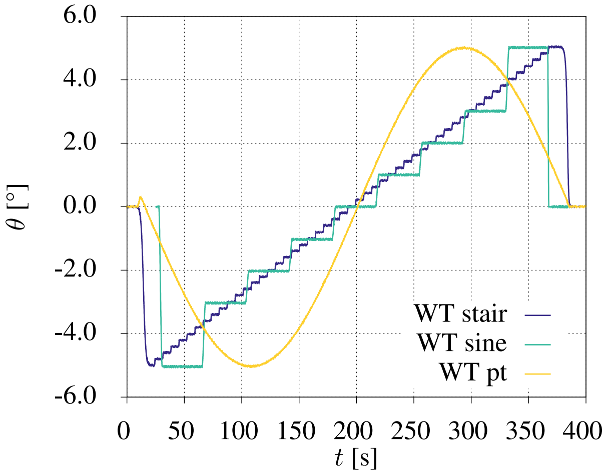

Fig. 11. Angle-of-attack time series employed in the experimental study.

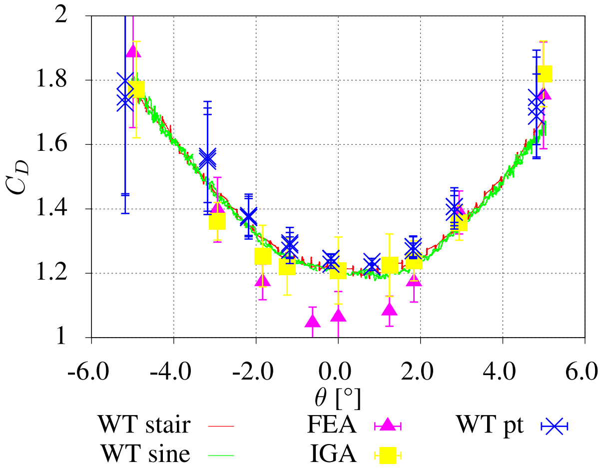

Fig. 12. Static drag coefficients C_D from wind tunnel experiments and numerical simulations for the R10 section.

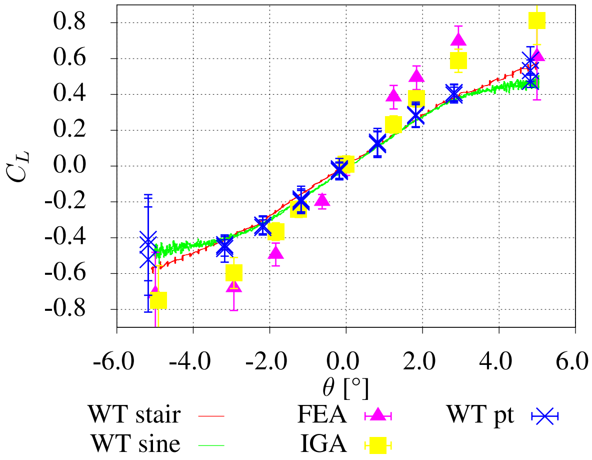

Fig. 13. Static lift coefficients C_L from wind tunnel experiments and numerical simulations for the R10 section.

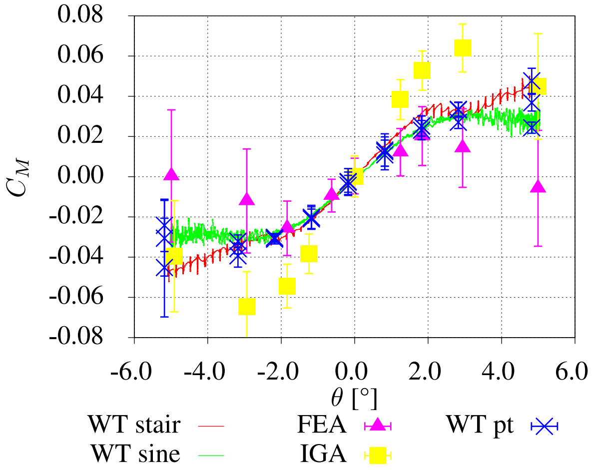

Fig. 14. Static moment coefficients C_M from wind tunnel experiments and numerical simulations for the R10 section.

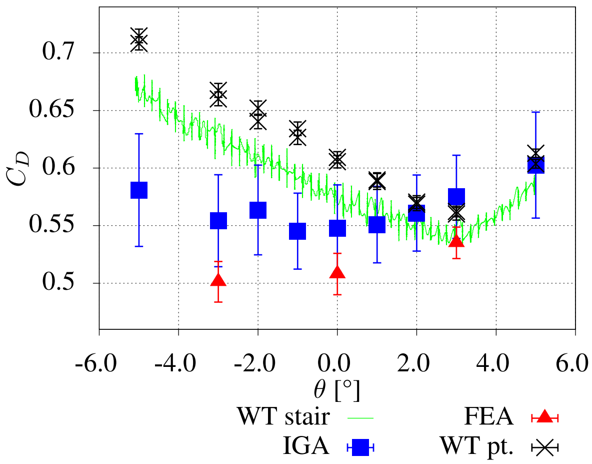

Fig. 15. Static drag coefficients C_D from wind tunnel experiments and numerical simulations for the Hardanger section.

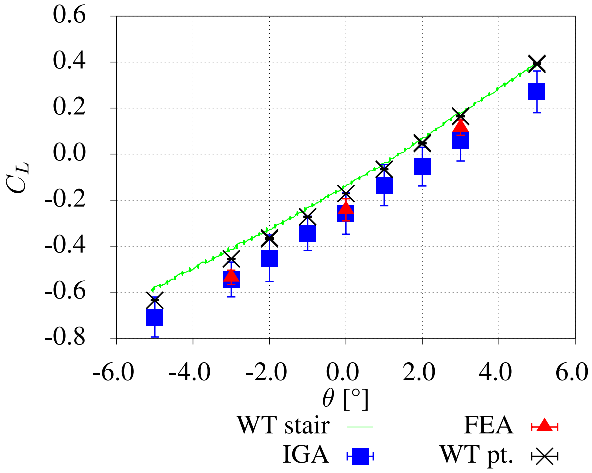

Fig. 16. Static lift coefficients C_L from wind tunnel experiments and numerical simulations for the Hardanger section.

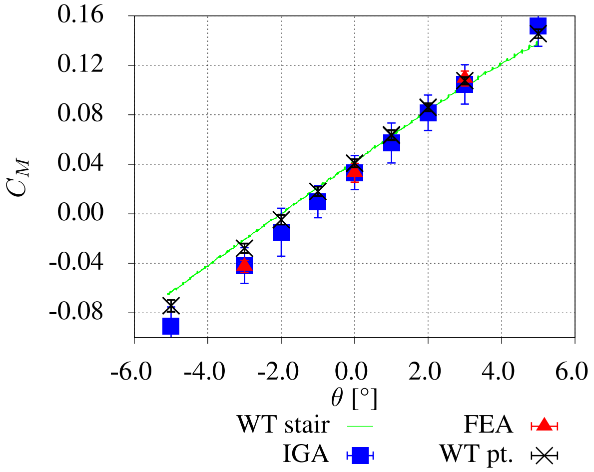

Fig. 17. Static moment coefficients C_M from wind tunnel experiments and numerical simulations for the Hardanger section.

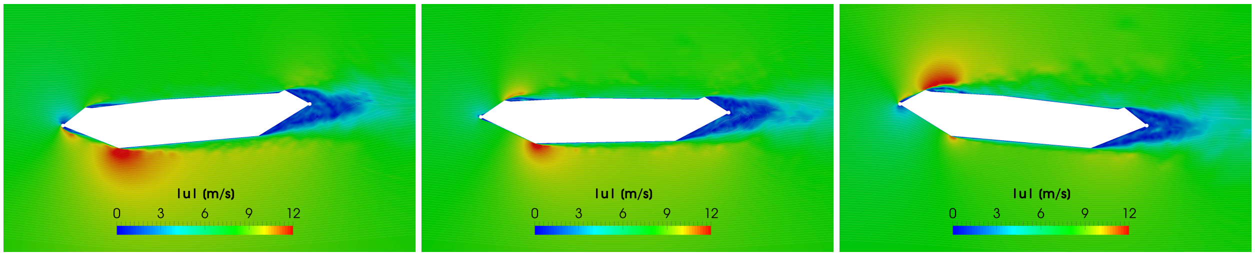

(a) θ = -5 ° **(b)** θ = 0 ° **(c)** θ = 5 °

Fig. 18. Velocity contours time-averaged over 0.25 s for the Hardanger section at different angles of attack.

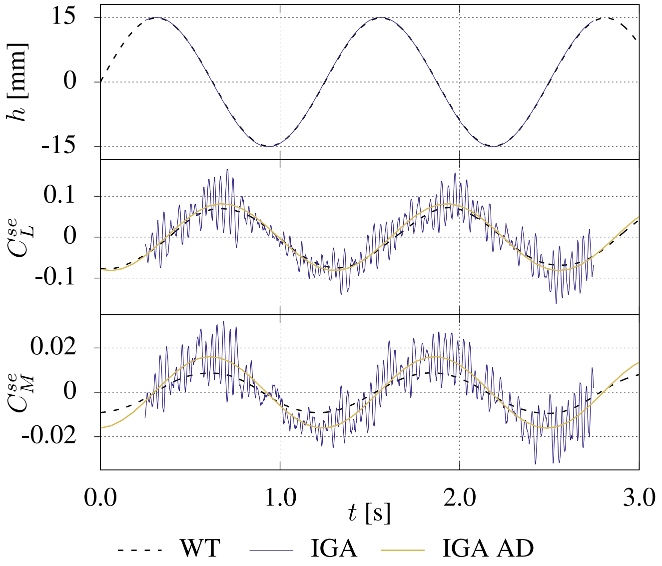

Fig. 19. Self-excited force coefficients for the vertical motion with $f = 0.8$ Hz and $U = 8$ m/s. Output from the IGA simulation compared to experimental results.

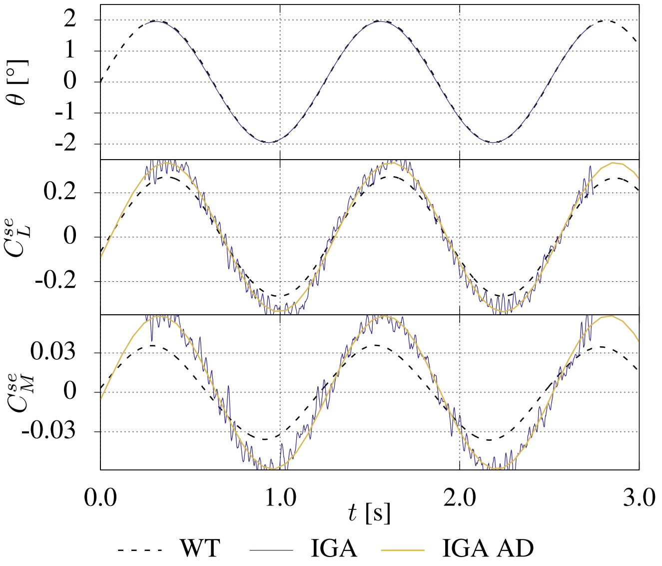

Fig. 20. Self-excited force coefficients for the pitching motion with $f = 0.8$ Hz and $U = 8$ m/s. Output from the IGA simulation compared to experimental results.

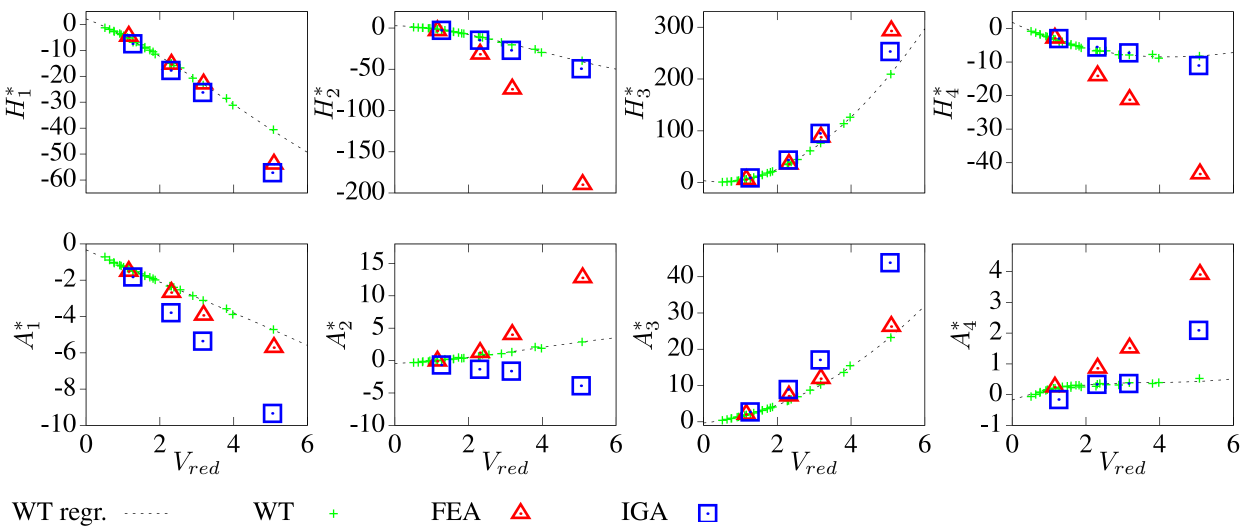

Fig. 21. Aerodynamic derivatives for the R10 section. The wind tunnel and FE results plotted are from (Helgedagsrud et al. 2018). The reduced velocity, $V_{red} = U/B\omega$, is defined in terms of the circular frequency.

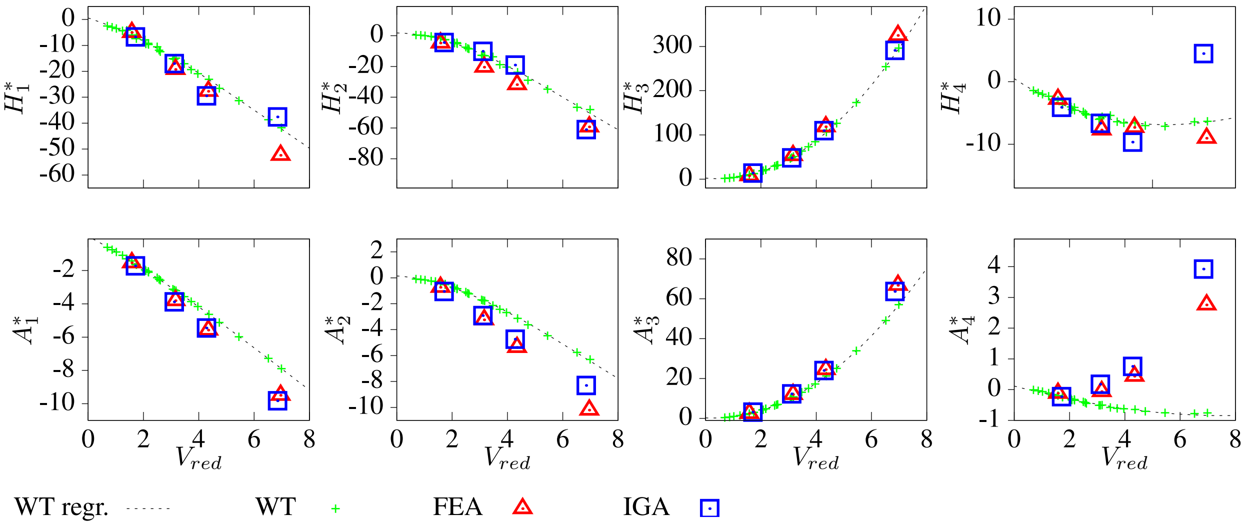

Fig. 22. Aerodynamic derivatives for the Hardanger bridge section. The wind tunnel and FE results are from (Helgedagsrud et al. 2018).